

Investigation of Spin Transport Properties in Perpendicularly Magnetized MoS₂/Pt/[Co/Ni]_n Multilayers with Effective Spin Injection into Two-Dimensional MoS₂

Shaohai Chen,¹ Guanjie Wu,² Qidong Xie,¹ Jing Zhou,¹ Xinyu Shu,¹ Zongzhi Zhang,² and Jingsheng Chen^{1,*}

¹*Department of Materials Science and Engineering, National University of Singapore, Singapore, 117576, Singapore*

²*Key Lab of Micro and Nano Photonic Structures (Ministry of Education), Department of Optical Science and Engineering, Fudan University, Shanghai, 200433, China*



(Received 13 May 2020; accepted 15 July 2020; published 30 July 2020)

Injecting spin current from ferromagnetic metals into two-dimensional (2D) transition-metal dichalcogenide semiconductors is expected to trigger a revolution in the next generation of energy-efficient spintronic and valleytronic devices. By investigating the spin transport properties in perpendicularly magnetized MoS₂/Pt/[Co/Ni]₂ and MoS₂/Pt/Ni/[Co/Ni]₂ heterostructures, here we demonstrate a strong and controllable spin injection into the 2D MoS₂ layer through a nonmagnetic Pt layer. Based on optical dynamic measurements, noticeable changes in the magnetic damping constant show that the spin injection intensity can be controlled by the Pt layer thickness. The improved spin mixing conductance of the interface is much higher than those reported in Pt/Ni/permalloy (Py) systems with in-plane magnetic anisotropy. Our results shed lights on the development of next-generation low-power spintronic devices employing both perpendicular magnetic anisotropy and 2D material.

DOI: 10.1103/PhysRevApplied.14.014095

I. INTRODUCTION

In traditional electronics, information processing is based on the physical migration of electrons, which inevitably causes Joule heating, and thus, energy loss. Spintronic devices, such as spin-torque magnetic random access memory and nano-oscillators, utilize the spin degree of freedom of electrons to encode and process information, enabling lower energy consumption due to less charge movement [1–5]. The generation and control of pure spin current has stimulated extensive investigations in nonmagnetic metal-ferromagnetic (NM-FM) bilayer systems in the last decade [6–18]. In certain multivalley semiconductors, it is proposed that information encoding can be achieved by confining charge carriers in different local minima (“valleys”) in the conduction band [19,20], which leads to the realization of valleytronic devices [20,21]. The two-dimensional (2D) transition-metal dichalcogenide (TMD) semiconductor, such as MoS₂, has exhibited promising prospects in both spin- and valleytronics due to exotic electronic and optical properties. For example, monolayer MoS₂ exhibits highly efficient spin-to-charge conversion [22,23] and optically excited spin-valley polarization [24]. A large Rashba-Edelstein effect

inducing spin-orbit torque (SOT) [25] and strong magnetic damping modification [26–28] are also observed in MoS₂/FM bilayers. Moreover, when charge carriers move in the 2D TMD, theoretical studies predict full out-of-plane spin polarization in both conduction and valence bands due to a strong Rashba-Edelstein effect [29]. This out-of-plane spin polarization can be injected into and detected by a FM layer possessing perpendicular magnetic anisotropy (PMA) to develop spin-based valleytronics. Our previous work shows that the integration of TMD and FM materials with strong PMA can be achieved in the MoS₂/Pt/[Co/Ni]₂ heterostructure [30]. However, studies on the spin transport properties in a perpendicularly magnetized TMD-FM bilayer are still missing.

Here, we fabricate perpendicularly magnetized FM multilayers on a MoS₂ layer with the structures of MoS₂/Pt/[Co/Ni]₂ and MoS₂/Pt/Ni/[Co/Ni]₂. The all-optical time-resolved magneto-optical Kerr effect (TR MOKE) technique is used to evaluate the influence of spin pumping in the two series of samples. Compared with the spin-torque ferromagnetic resonance and spin Hall magnetoresistance measurements, the noninvasive all-optical pump-and-probe technique provides a more precise magnetic damping measurement, since no microfabrication is required and the inhomogeneity-induced extrinsic damping contribution can be excluded [31]. In analyzing both

* msecj@nus.edu.sg

static and dynamic measurement results, we show that the strong magnetic proximity effect exists only in samples with the Pt/Co interface. For samples with the Pt/Ni interface, magnetic damping shows an abnormal increase when the Pt layer thickness is smaller than that of its spin diffusion length, which is attributed to the combined effects of enhanced orbital hybridization at the Pt/Ni interface and strong spin injection at the MoS₂/Pt interface. Due to the MoS₂ layer, the spin mixing conductance of the Pt/Ni interface is enhanced twofold. These results will motivate the development of perpendicularly magnetized TMD-FM systems for low-power spintronic and valleytronic devices.

II. EXPERIMENTAL DETAILS

It is shown in our previous work that MoS₂ can strongly enhance orbital hybridization at the Pt/Co interface in the MoS₂/Pt/[Co/Ni]₂ heterostructures when the Pt layer thickness (t_{Pt}) is smaller than 5 nm [30]. However, orbital hybridization at the Pt/Co interface may lead to proximity-induced magnetic moments [31], which result in interface spin-flip scattering and induce magnetic damping enhancement of complicated origins. To better understand the spin transport properties in the perpendicularly magnetized MoS₂/Pt/FM system, two series of samples are fabricated: (A) Si(SiO₂) substrate/MoS₂(2L)/Pt(0.5–15)/[Co(0.28)/Ni(0.56)]₂/SiO₂(4), and (B) Si(SiO₂) substrate/MoS₂(2L)/Pt(0.5–15)/Ni(0.56)/[Co(0.28)/Ni(0.56)]₂/SiO₂, where MoS₂ is two monolayers (2L) thick (around 0.65 nm) and the values in parentheses are in nm. For simplicity, the two series of samples are hereafter referred to as MoS₂/Pt/Co and MoS₂/Pt/Ni samples, respectively. The MoS₂ layer is fabricated in a separated sputtering chamber by utilizing a Mo metal target under a vaporized sulfur atmosphere, with heating of the substrate to 700 °C. All other layers are fabricated in another sputtering chamber at room temperature, where the deposition rates of Pt, Co, Ni, and SiO₂ are 0.15, 0.048, 0.046, and 0.02 nm/s, respectively. The base vacuum pressure of the sputtering chamber is 1×10^{-9} torr.

The magnetic hysteresis loops of all samples are measured by a vibrating sample magnetometer (VSM) system. The TR MOKE measurements are carried out by using a pulsed Ti:sapphire laser with a central wavelength of 800 nm. The pulse duration is 150 fs and the repetition rate is 1000 Hz. The pump pulse launches the magnetic moment, m , to precess around the effective field, H_{eff} , which is determined by the external field, H_{ex} , and the effective PMA field, H_{eff} , and the probe pulse detects the polar Kerr rotation as a function of time delay Δt . Both the pump-and-probe laser pulses are perpendicular incidence to the film plane, of which the fluences are about 0.60 and 0.05 mJ/cm². During the measurements, H_{ex} is applied at a fixed angle of 71° with respect to the film normal.

III. RESULTS AND DISCUSSION

A. Measurements of static magnetic properties

In the static magnetic properties measurements, as shown in the Supplemental Material [32], the magnetic hysteresis loops results confirm that all samples possess good PMA. To exclude the influence of MoS₂, Fig. 1(a) shows the saturated magnetization, M_s ; the PMA field, H_k ; and the PMA constant, $K_u = [(H_k M_s)/2] + 2\pi M_s^2$, of the MoS₂/Pt/Co and MoS₂/Pt/Ni samples when $t_{\text{Pt}} = 15$ nm. The MoS₂/Pt/Co sample possesses a K_u of $(\sim 5.34 \pm 0.1) \times 10^6$ erg/cm³, which is higher than that of

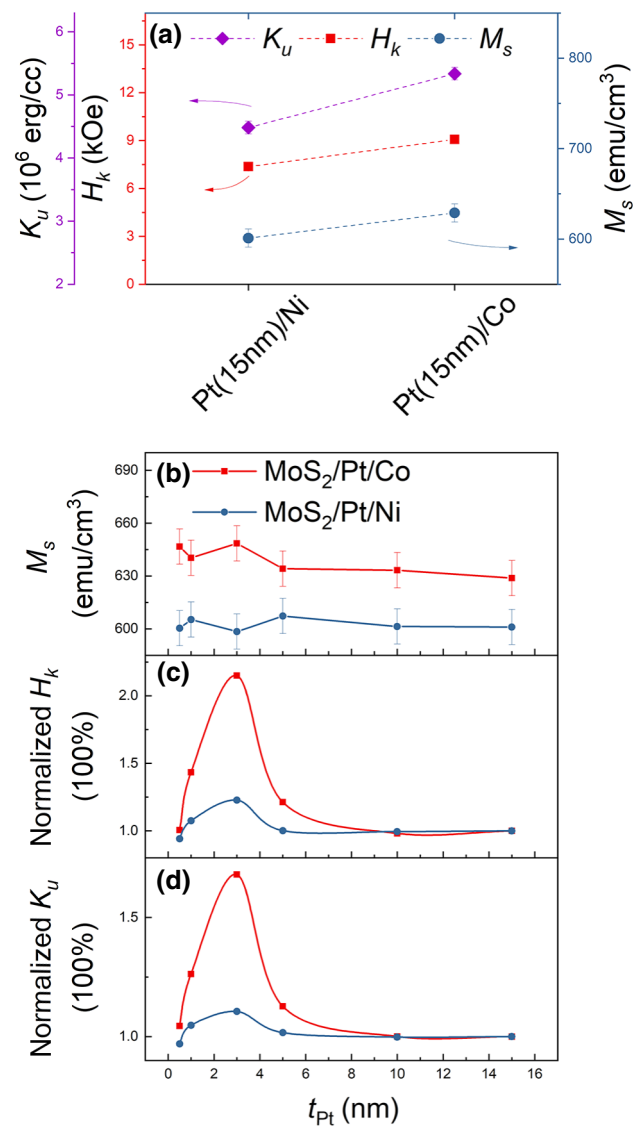


FIG. 1. (a) Saturated magnetization (M_s), magnetic anisotropy field (H_k), and intrinsic magnetic anisotropy energy (K_u) of MoS₂/Pt/Co and MoS₂/Pt/Ni samples with $t_{\text{Pt}} = 15$ nm. (b)–(d) Dependences of M_s , normalized H_k , and normalized K_u , respectively, on t_{Pt} of MoS₂/Pt/Co and MoS₂/Pt/Ni samples. Normalization is based on the sample with $t_{\text{Pt}} = 15$ nm.

the MoS₂/Pt/Ni sample of ($\sim 4.48 \pm 0.1$) $\times 10^6$ erg/cm³. This is attributed to the interfacial hybridization of Co-Pt, where extra PMA is induced [33]. Figure 1(b) shows M_s variation of the two series of samples with different t_{Pt} . The M_s values of all MoS₂/Pt/Ni samples remains at (601 \pm 5) emu/cm³, which is comparable to the intrinsic $M_s \sim 600$ emu/cm³ of the [Co/Ni]_n multilayer structure [34]. However, the M_s value of the MoS₂/Pt/Co samples is stable at (630 \pm 5) emu/cm³, when $t_{\text{Pt}} \geq 5$ nm, and increases to (645 \pm 5) emu/cm³, when $t_{\text{Pt}} < 5$ nm. These values imply a substantial amount of proximity-induced magnetic moments in the MoS₂/Pt/Co samples, which are strengthened by the enhanced orbital hybridization at the Pt/Co interface caused by the MoS₂ layer [30,31]. Figures 1(c) and 1(d) show the dependence of normalized H_k and K_u , respectively, of the MoS₂/Pt/Co and MoS₂/Pt/Ni samples on t_{Pt} . Compared with the MoS₂/Pt/Co samples, the normalized H_k and K_u of the MoS₂/Pt/Ni samples show similar trends with a decrease of t_{Pt} . According to our previous results [30], the improved H_k and K_u in the MoS₂/Pt/Ni samples when $t_{\text{Pt}} < 5$ nm indicate that the MoS₂ layer also causes an enhanced orbital hybridization at the Pt/Ni interface. However, these increases in H_k and K_u are smaller than those in the case of MoS₂/Pt/Co samples, since the orbital hybridization enhancement at the Pt/Ni interface caused by MoS₂ is weaker [35].

B. TR MOKE measurements of the MoS₂/Pt/Co and MoS₂/Pt/Ni samples

Figure 2(a) and 2(b) show the TR MOKE measurement configuration and the TR MOKE spectrum, respectively, of the MoS₂/Pt/Ni sample with $t_{\text{Pt}} = 0.5$ nm measured when an external magnetic field of $H_{\text{ex}} = 15$ kOe is applied. After the pump-laser pulse, the TR MOKE spectra of all Pt/Co and Pt/Ni samples display similar ultrafast demagnetization, fast remagnetization, and slow relaxation processes, as shown by the shaded area and fitting line in Fig. 2(b). This indicates that, in the TR MOKE measurements, all samples possess similar energy-transfer processes between the electron, spin, and lattice [36]. By subtracting these components, Figs. 2(c) and 2(d) show the pure magnetization-precession-related TR MOKE spectra of the MoS₂/Pt/Co and MoS₂/Pt/Ni samples, respectively, when $t_{\text{Pt}} = 0.5$ nm and $H_{\text{ex}} = 6$ –15 kOe. Before carrying out the fitting processes, we perform fast-Fourier transforms (FFTs) on all TR MOKE spectra to check the precession modes. As shown in Fig. 2(e), the FFT power spectra of the MoS₂/Pt/Ni samples show a symmetrical single-frequency peak (f_{uni}), which indicates a uniform precession mode. While, for the MoS₂/Pt/Co sample, an additional frequency peak (f_{add}) starts to appear when H_{ex} is less than 10 kOe. As shown in the Supplemental Material [32], double-frequency-peak phenomena are also observed in the MoS₂/Pt/Co samples when $t_{\text{Pt}} = 1$

and 3 nm. With an increase of H_{ex} , it can be noted that f_{add} does not horizontally shift like f_{uni} . So, the additional precession mode is not derived from the interlayer-exchange-coupling-induced out-of-phase spin precession, which is generally observed in FM-FM systems with a weak ferromagnetic exchange coupling or FM-NM-FM systems with an antiferromagnetic exchange coupling [31, 37,38]. According to the M_s and H_k enhancements of the MoS₂/Pt/Co samples when $t_{\text{Pt}} < 5$ nm, f_{add} is attributed to magnetization inhomogeneities and the field-dragging effect [39]. When H_{ex} is relatively small, the magnetic moments at the Pt/Co interface precess at an independent frequency. When H_{ex} is large enough, f_{add} is suppressed because the magnetic moments are aligned in one direction and precess together. Because the maximum H_{ex} in our TR MOKE measurement is smaller than 15 kOe, we focus on the TR MOKE spectra of the MoS₂/Pt/Ni samples to discuss the spin transport properties.

Based on the uniform precession of the Kittel mode, the TR MOKE spectra of all MoS₂/Pt/Ni samples are fitted by the damped harmonic function:

$$M(t) = M(0)\exp(-t/\tau)\sin(2\pi ft + \phi), \quad (1)$$

where f , τ , and ϕ are the precession frequency, lifetime, and initial phase, respectively. It can be seen in Fig. 2(d) that the data points are well fitted by Eq. (1). The effective damping constant, α_{eff} , is calculated from $\alpha_{\text{eff}} = 1/(2\pi f\tau)$ [40]. Figures 3(a)–3(f) show α_{eff} versus H_{ex} curves of the MoS₂/Pt/Ni samples. When H_{ex} is smaller than 10 kOe, the increase of α_{eff} is because local magnetization fluctuations induce extrinsic contributions to magnetic damping. By fitting the curves with the decaying exponential function of $\alpha_{\text{eff}} = C_1 \exp(-H_{\text{ex}}/H_0) + \alpha_s$ [41], where C_1 and H_0 are the function coefficients, the saturated damping constant, α_s , at an infinite H_{ex} is obtained. In the MoS₂/Pt/Ni samples, all Ni layers above the Pt layer have the same thickness, so the [Ni/Co/Ni/Co/Ni] layers act as a whole FM layer [14]. It can be found in our previous results that the roughness of the MoS₂/Pt surface is small ($R_q \sim 0.4$ nm) and does not change with t_{Pt} [30]. As a result, α_s of the MoS₂/Pt/Ni samples is considered to be mainly derived from the intrinsic magnetic damping (α_{in}) of the [Co/Ni]_n multilayer structure and extrinsic damping increase ($\Delta\alpha_{\text{ex}}$) caused by the spin-pumping effect. Figure 3(g) shows the α_s versus t_{Pt} curves of the MoS₂/Pt/Ni samples. With an increase of t_{Pt} , α_s increases to a maximum when $t_{\text{Pt}} = 3$ nm and becomes steady when $t_{\text{Pt}} \geq 10$ nm. This is quite different from the reported phenomena in Pt(or MoS₂)/FM bilayer systems, where α_s monotonically increases to saturation with increasing NM layer thickness [26,42]. Considering the PMA variation of the MoS₂/Pt/Ni samples, the orbital hybridization enhancement at the Pt/Ni interface can be one reason for the nonmonotonic α_s increase, which

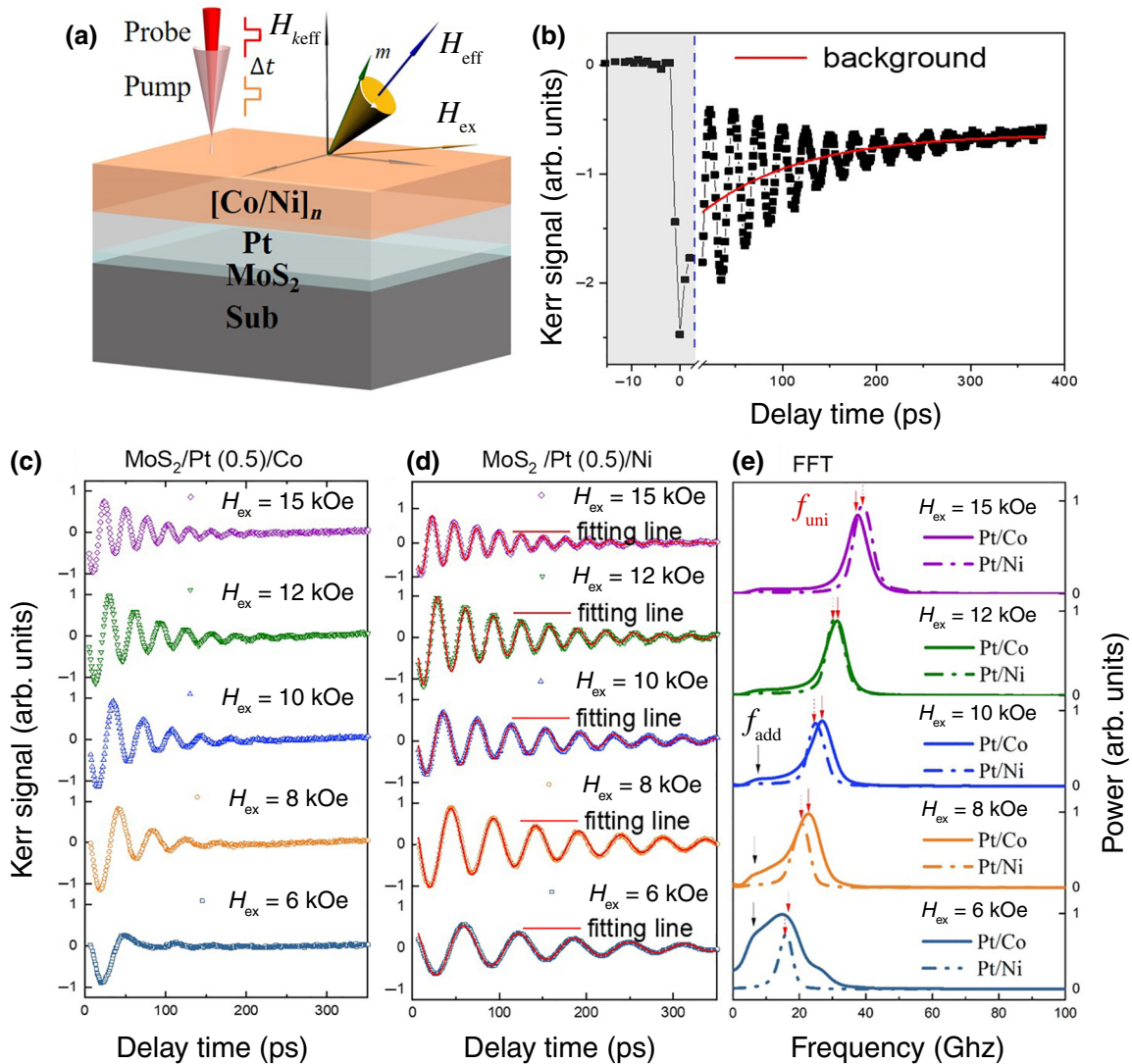


FIG. 2. (a) Scheme of the TR MOKE measurement configuration. (b) TR MOKE spectrum of MoS₂/Pt/Ni sample when $t_{\text{Pt}} = 0.5 \text{ nm}$ and $H_{\text{ex}} = 15 \text{ kOe}$. Background line represents slow relaxation caused by heat diffusion. (c)–(e) Processed TR MOKE spectra and corresponding FFT power spectra of MoS₂/Pt/Co and MoS₂/Pt/Ni samples when $t_{\text{Pt}} = 0.5 \text{ nm}$ and $H_{\text{ex}} = 6\text{--}15 \text{ kOe}$, respectively.

induces extra $\Delta\alpha_{\text{ex}}$ by increasing the interfacial spin transparency and enhancing the spin-injection intensity [43,44]. However, according to the much larger variation of normalized α_s , it suggests that the increase of α_s may have other contributions.

It was reported that optical excitation could lead to a strong spin injection from the FM layer into a semiconductor [23,45]. Corresponding to our system, the experimental results can be rationalized when spin injection at the MoS₂/Pt interface is considered. In TR MOKE measurements, magnetization precession in the [Co/Ni]_n multilayer causes a spin current to flow into the Pt layer. When t_{Pt} is larger than its spin-diffusion length (λ_{Pt}), as shown in Fig. 4(a), the angular momentum of the injected spins in the Pt layer is completely dephased by the spin-flip

scattering. According to the spin-pumping model [6], continuous spin injection from the FM layer into the Pt layer leads to a magnetic damping increase ($\Delta\alpha_{\text{Pt}}$), where the injected spin current is generally known as I_{pump} and named $I_{p,\text{Pt}}$ here. When t_{Pt} approaches λ_{Pt} , as shown in Fig. 4(b), on one hand, enhanced orbital hybridization at the Pt/Ni interface leads to a larger $I_{p,\text{Pt}}$. On the other hand, those injected spins in the Pt layer with an excitation energy higher than that of the MoS₂ conduction band minimum will further go across the MoS₂/Pt interface and inject into MoS₂. We name this injected spin current I_{p,MoS_2} . Enhanced $I_{p,\text{Pt}}$ and the presence of I_{p,MoS_2} result in a large magnetic damping increase ($\Delta\alpha_{\text{MoS}_2/\text{Pt}}$). With a further decrease of t_{Pt} , as shown in Fig. 4(c), the spin-accumulation effect makes the injected spins flow

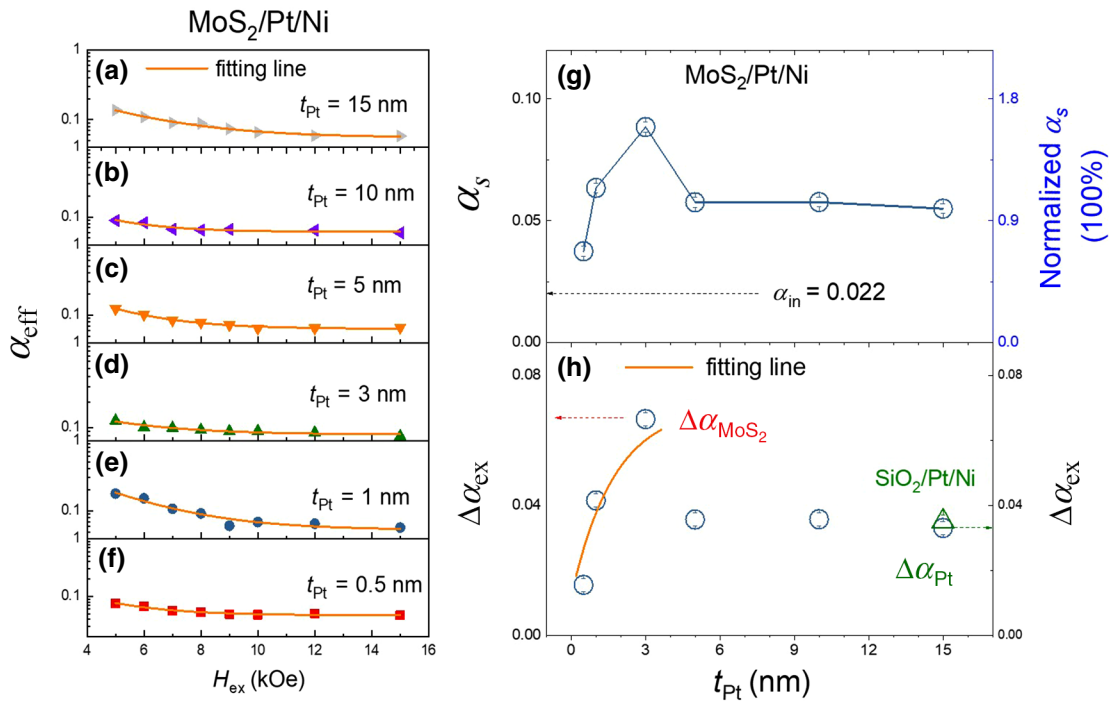


FIG. 3. (a)–(f) Effective magnetic damping, α_{eff} , versus H_{ex} curves of MoS₂/Pt/Ni samples when $t_{\text{Pt}} = 15$ –0.5 nm. (g),(h) Saturated effective magnetic damping, α_s , and damping increase, $\Delta\alpha_{\text{eff}}$, versus t_{Pt} curves, respectively, of MoS₂/Pt/Ni samples.

back to the [Co/Ni]₂ multilayer [42]. The generated back-flow spin current (I_{back}) causes the decrease in magnetic damping.

When a spin current crosses the NM-FM interface, the nonlocal magnetic damping variation can be evaluated by the interfacial effective spin-mixing conductance, G_{eff} , or intrinsic spin-mixing conductance, $G_{\uparrow\downarrow}$. The difference is that G_{eff} considers I_{back} and $G_{\uparrow\downarrow}$ does not, which makes $G_{\uparrow\downarrow}$ relatively large. In the case of the MoS₂/Pt underlayer, the dependence of G_{eff} on $\Delta\alpha_{\text{ex}}$ (and thus, $G_{\uparrow\downarrow}$) can be given as follows [15]:

$$G_{\text{eff}} = \frac{4\pi M_s t_{\text{FM}}}{g\mu_B} \Delta\alpha_{\text{ex}} = \frac{4\pi M_s t_{\text{FM}}}{g\mu_B} (\alpha_s - \alpha_{\text{in}}), \quad (2)$$

$$\Delta\alpha_{\text{ex}} = \frac{g\mu_B}{4\pi M_s t_{\text{FM}}} G_{\uparrow\downarrow} \left[1 - \exp \left(-\frac{2t_{\text{Pt}} + t_{\text{MoS}_2}}{\lambda} \right) \right], \quad (3)$$

where g and μ_B are the Landé g factor and Bohr magneton, respectively. Based on the Kittel formula, $2\pi f = [\gamma_e g]/2\sqrt{H_1 H_2}$, where $\gamma_e = 1.76 \times 10^7 \text{ Hz/Oe}$ and H_1 and H_2 are H_{ex} -related parameters [32], the g factor of the Pt/Ni samples is 1.94 ± 0.06 . To calculate G_{eff} , we take the reported value of $\alpha_{\text{in}} = 0.022$ of the Co/Ni multilayer structure to obtain $\Delta\alpha_{\text{ex}}$ [46]. From the $\Delta\alpha_{\text{ex}}$ versus t_{Pt} curve, as shown Fig. 3(h), $\Delta\alpha_{\text{Pt}}$ and $\Delta\alpha_{\text{MoS}_2/\text{Pt}}$ are obtained as 0.034 ± 0.002 and 0.067 ± 0.002 , respectively. To confirm that $\Delta\alpha_{\text{Pt}}$ is not influenced by MoS₂, we find $\Delta\alpha_{\text{ex}} = 0.035 \pm 0.002$ for a control sample with

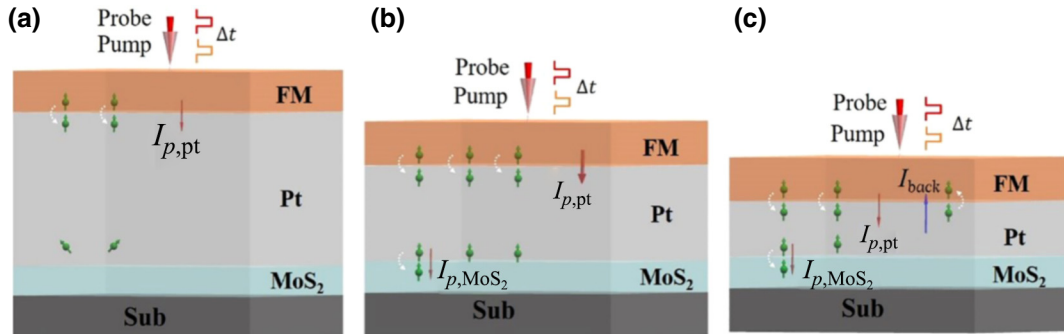


FIG. 4. (a)–(c) Scheme of spin transport processes in MoS₂/Pt underlayer when t_{Pt} is larger than, close to, and smaller than the spin diffusion length of Pt, respectively.

the structure of $\text{SiO}_2/\text{Pt}(15 \text{ nm})/\text{Ni}/[\text{Co}/\text{Ni}]_2$, as shown in Fig. 3(h). This agrees well with the $\text{MoS}_2/\text{Pt}/\text{Ni}$ sample with $t_{\text{Pt}} = 15 \text{ nm}$. According to Eq. (2), $G_{\text{eff},\text{Pt}/\text{Ni}}$ is calculated to be (33.5 ± 1.2) and $(66.1 \pm 1.2) \text{ nm}^{-2}$ with and without the MoS_2 contribution, respectively. In the $\text{MoS}_2/\text{permalloy}(\text{Py})$ and Pt/Py bilayer systems with in-plane anisotropy, the reported $G_{\text{eff},\text{MoS}_2/\text{Py}} = 3.1\text{--}29.3 \text{ nm}^{-2}$ and $G_{\text{eff},\text{Pt}/\text{Py}} = 15.2\text{--}30 \text{ nm}^{-2}$ are all smaller than our $G_{\text{eff},\text{Pt}/\text{Ni}}$ value, when spin injection exists only in the Pt layer [6,27,44,47,48]. Pai *et al.* [49] show that G_{eff} of the Pt/FM system is strongly related to interfacial conditions, such as crystal structure and magnetic anisotropy. Zink *et al.* [43] show that, when there is an out-of-plane component of magnetic anisotropy at the Pt/Ni interface, G_{eff} can be efficiently enhanced. Hence, the relatively higher $G_{\text{eff},\text{Pt}/\text{Ni}}$ value in our $\text{MoS}_2/\text{Pt}/\text{Ni}$ sample is attributed to the difference in the interfacial magnetic anisotropies in different material systems. Using $G_{\uparrow\downarrow,\text{Pt}/\text{Ni}} > (66.1 \pm 1.2) \text{ nm}^{-2}$ and Eq. (3), we find that the effective spin-diffusion length, λ , of the MoS_2/Pt bilayer is larger than $(3.4 \pm 0.4) \text{ nm}$. At the same time, since $\Delta\alpha_{\text{ex}}$ of $\text{MoS}_2/\text{Pt}/\text{Ni}$ is unchanged when $t_{\text{Pt}} \geq 5 \text{ nm}$, it suggests that the effective λ of the MoS_2/Pt bilayer is smaller than 5 nm . Both the maximum and minimum values of λ are within the reported range of $\lambda_{\text{Pt}} = 1.4\text{--}11.0 \text{ nm}$ obtained in Pt/Py bilayer systems [42,50].

IV. CONCLUSIONS

We explore the spin transport properties of perpendicularly magnetized $\text{MoS}_2/\text{Pt}/[\text{Co}/\text{Ni}]_2$ and $\text{MoS}_2/\text{Pt}/\text{Ni}/[\text{Co}/\text{Ni}]_2$ heterostructures. For the $\text{MoS}_2/\text{Pt}/\text{Co}$ samples, the proximity-induced magnetic moments and enhanced PMA at the Pt/Co interface lead to multiple magnetization precession modes in the TR MOKE measurement, which result in a mixed contribution to the effective magnetic damping constant. Based on the $\text{MoS}_2/\text{Pt}/\text{Ni}$ samples with different Pt thicknesses, we find the MoS_2 layer not only causes an enhanced orbital hybridization at the Pt/Ni interface, but also serves as a good spin sink for the injected spin current from the MoS_2/Pt interface. Compared with the perpendicularly magnetized $\text{SiO}_2/\text{Pt}/\text{Ni}/[\text{Co}/\text{Ni}]_2$ structure, the spin mixing conductance of the Pt/Ni interface of the $\text{MoS}_2/\text{Pt}/\text{Ni}$ samples is substantially enhanced from (33.5 ± 1.2) to $(66.1 \pm 1.2) \text{ nm}^{-2}$. Our results demonstrate the opportunity of integrating the advantages of PMA and TMD materials, which can be an effective route for the development of energy-efficient spintronic or valleytronic devices.

ACKNOWLEDGMENTS

The research is supported by the Singapore Ministry of Education (Grants No. MOE2018-T2-1-019, No. MOE2018-T2-2-043, No. Tier 1 R284-000-195-114), A*STAR (Grants No. A1983c0036, No. IAF-ICP

1801E0036) and by National Natural Science Foundation of China (Grants No. 11874120 and No. 51671057). J.S.C. is a member of the Singapore Spintronics Consortium (SG-SPIN).

- [1] I. Žutić, J. Fabian, and S. Das Sarma, Spintronics: Fundamentals and applications, *Rev. Mod. Phys.* **76**, 323 (2004).
- [2] A. Brataas, A. D. Kent, and H. Ohno, Current-induced torques in magnetic materials, *Nat. Mater.* **11**, 372 (2012).
- [3] T. Jungwirth, J. Wunderlich, and K. Olejnik, Spin hall effect devices, *Nat. Mater.* **11**, 382 (2012).
- [4] A. Hoffmann and S. D. Bader, Opportunities at the Frontiers of Spintronics, *Phys. Rev. Appl.* **4**, 047001 (2015).
- [5] C. Chappert and J.-V. Kim, Electronics free of charge, *Nat. Phys.* **4**, 837 (2008).
- [6] Y. Tserkovnyak, A. Brataas, and G. E. W. Bauer, Spin pumping and magnetization dynamics in metallic multilayers, *Phys. Rev. B* **66**, 224403 (2002).
- [7] K. Uchida, S. Takahashi, K. Harii, J. Ieda, W. Koshibae, K. Ando, S. Maekawa, and E. Saitoh, Observation of the spin seebeck effect, *Nature* **455**, 778 (2008).
- [8] L. Liu, C.-F. Pai, Y. Li, H. W. Tseng, D. C. Ralph, and R. A. Buhrman, Spin-Torque switching with the giant spin Hall effect of tantalum, *Science* **336**, 555 (2012).
- [9] G. E. W. Bauer, E. Saitoh, and B. J. van Wees, Spin caloritronics, *Nat. Mater.* **11**, 391 (2012).
- [10] J. C. R. Sánchez, L. Vila, G. Desfonds, S. Gambarelli, J. P. Attané, J. M. De Teresa, C. Magén, and A. Fert, Spin-to-charge conversion using rashba coupling at the interface between non-magnetic materials, *Nat. Commun.* **4**, 2944 (2013).
- [11] A. Soumyanarayanan, N. Reyren, A. Fert, and C. Panagopoulos, Emergent phenomena induced by spin-orbit coupling at surfaces and interfaces, *Nature* **539**, 509 (2016).
- [12] L. Chico, P. A. Orellana, L. Rosales, and M. Pacheco, Spin and Charge Caloritronics in Bilayer Graphene Flakes with Magnetic Contacts, *Phys. Rev. Appl.* **8**, 054029 (2017).
- [13] W. Lin, S. D. Pollard, R. Guo, H. Y. Yoong, S. Chen, H. Wang, L. Liu, C. Li, X. Yu, J. Xiao, X. Chi, J. Yu, J. Zhou, T. Zhou, H. Yang, and J. Chen, Tuning of current-induced effective magnetic field through rashba effect engineering in hybrid multiferroic structures, *NPG Asia Mater.* **10**, 740 (2018).
- [14] S. Chen, J. Yu, Q. Xie, X. Zhang, W. Lin, L. Liu, J. Zhou, X. Shu, R. Guo, Z. Zhang, and J. Chen, Free field electric switching of perpendicularly magnetized thin film by spin current gradient, *ACS Appl. Mater. Interfaces* **11**, 30446 (2019).
- [15] S. N. Panda, S. Mondal, J. Sinha, S. Choudhury, and A. Barman, All-optical detection of interfacial spin transparency from spin pumping in $\beta\text{-Ta}/\text{CoFeB}$ thin films, *Sci. Adv.* **5**, eaav7200 (2019).
- [16] L. Liu, Q. Qin, W. Lin, C. Li, Q. Xie, S. He, X. Shu, C. Zhou, Z. Lim, J. Yu, W. Lu, M. Li, X. Yan, S. J. Pennycook, and J. Chen, Current-induced magnetization switching in all-oxide heterostructures, *Nat. Nanotech.* **14**, 939 (2019).

- [17] J. Zhou, X. Wang, Y. Liu, J. Yu, H. Fu, L. Liu, S. Chen, J. Deng, W. Lin, X. Shu, H. Y. Yoong, T. Hong, M. Matsuda, P. Yang, S. Adams, B. Yan, X. Han, and J. Chen, Large spin-orbit torque efficiency enhanced by magnetic structure of collinear antiferromagnet IrMn, *Sci. Adv.* **5**, eaau6696 (2019).
- [18] X. Shu, J. Zhou, J. Deng, W. Lin, J. Yu, L. Liu, C. Zhou, P. Yang, and J. Chen, Spin-orbit torque in chemically disordered and L₁₁-ordered Cu_{100-x}Pt_x, *Phys. Rev. Mater.* **3**, 114410 (2019).
- [19] V. L. Gurevich and A. Thellung, Quasimomentum in the theory of elasticity and its conservation, *Phys. Rev. B Condens Matter* **42**, 7345 (1990).
- [20] A. Rycerz, J. Tworzydło, and C. W. J. Beenakker, Valley filter and valley valve in graphene, *Nat. Phys.* **3**, 172 (2007).
- [21] J. R. Schaibley, H. Yu, G. Clark, P. Rivera, J. S. Ross, K. L. Seyler, W. Yao, and X. Xu, Valleytronics in 2D materials, *Nat. Rev. Mater.* **1**, 16055 (2016).
- [22] J. B. S. Mendes, A. Aparecido-Ferreira, J. Holanda, A. Azevedo, and S. M. Rezende, Efficient spin to charge current conversion in the 2D semiconductor MoS₂ by spin pumping from yttrium iron garnet, *Appl. Phys. Lett.* **112**, 242407 (2018).
- [23] L. Cheng, X. Wang, W. Yang, J. Chai, M. Yang, M. Chen, Y. Wu, X. Chen, D. Chi, K. E. J. Goh, J.-X. Zhu, H. Sun, S. Wang, J. C. W. Song, M. Battiatto, H. Yang, and E. E. M. Chia, Far out-of-equilibrium spin populations trigger giant spin injection into atomically thin MoS₂, *Nat. Phys.* **15**, 347 (2019).
- [24] K. F. Mak, K. He, J. Shan, and T. F. Heinz, Control of valley polarization in monolayer MoS₂ by optical helicity, *Nat. Nanotech.* **7**, 494 (2012).
- [25] Q. Shao, G. Yu, Y.-W. Lan, Y. Shi, M.-Y. Li, C. Zheng, X. Zhu, L.-J. Li, P. K. Amiri, and K. L. Wang, Strong rashba-edelstein effect-induced spin–orbit torques in monolayer transition metal dichalcogenide/ferromagnet bilayers, *Nano Lett.* **16**, 7514 (2016).
- [26] S. Husain, A. Kumar, P. Kumar, A. Kumar, V. Barwal, N. Behera, S. Choudhary, P. Svedlindh, and S. Chaudhary, Spin pumping in the heusler alloy Co₂FeAl/MoS₂ heterostructure: Ferromagnetic resonance experiment and theory, *Phys. Rev. B* **98**, 180404(R) (2018).
- [27] R. Bansal, A. Kumar, N. Chowdhury, N. Sisodia, A. Barvat, A. Dogra, P. Pal, and P. K. Muduli, Extrinsic spin-orbit coupling induced enhanced spin pumping in few-layer MoS₂/Py, *J. Magnetism Magnetic Mater.* **476**, 337 (2019).
- [28] G. Wu, Y. Ren, X. He, Y. Zhang, H. Xue, Z. Ji, Q. Y. Jin, and Z. Zhang, Tuning Magnetization Dynamics with Strong Spin-Orbit Coupling in Transition-Metal Dichalcogenide/Co-Fe-B Heterostructures, *Phys. Rev. Appl.* **13**, 024027 (2020).
- [29] Z. Y. Zhu, Y. C. Cheng, and U. Schwingenschlögl, Giant spin-orbit-induced spin splitting in two-dimensional transition-metal dichalcogenide semiconductors, *Phys. Rev. B* **84**, 153402 (2011).
- [30] Q. Xie, W. Lin, B. Yang, X. Shu, S. Chen, L. Liu, X. Yu, M. B. H. Breese, T. Zhou, M. Yang, Z. Zhang, S. Wang, H. Yang, J. Chai, X. Han, and J. Chen, Giant enhancements of perpendicular magnetic anisotropy and spin-orbit torque by a MoS₂ layer, *Adv. Mater.* **31**, 1900776 (2019).
- [31] M. Caminale, A. Ghosh, S. Auffret, U. Ebels, K. Ollefs, F. Wilhelm, A. Rogalev, and W. E. Bailey, Spin pumping damping and magnetic proximity effect in Pd and Pt spin-sink layers, *Phys. Rev. B* **94**, 014414 (2016).
- [32] See the Supplemental Material at <http://link.aps.org/supplemental/10.1103/PhysRevApplied.14.014095> for more details on magnetic hysteresis loops of all samples, the FFT power spectra of the samples with t_{Pt}>0.5nm, and the f versus H_{ex} curves of the MoS₂/Pt/Ni samples, respectively.
- [33] D. Weller, Y. Wu, J. Stohr, M. G. Samant, B. D. Hermsmeier, and C. Chappert, Orbital magnetic moments of Co in multilayers with perpendicular magnetic anisotropy, *Phys. Rev. B Condens Matter* **49**, 12888 (1994).
- [34] M. Arora, R. Hübner, D. Suess, B. Heinrich, and E. Girt, Origin of perpendicular magnetic anisotropy in Co/Ni multilayers, *Phys. Rev. B* **96**, 024401 (2017).
- [35] S. Sahoo, A. Hucht, M. E. Gruner, G. Rollmann, P. Entel, A. Postnikov, J. Ferrer, L. Fernández-Seivane, M. Richter, D. Fritsch, and S. Sil, Magnetic properties of small Pt-capped Fe, Co, and Ni clusters: A density functional theory study, *Phys. Rev. B* **82**, 054418 (2010).
- [36] E. Beaurepaire, J. C. Merle, A. Daunois, and J. Y. Bigot, Ultrafast Spin Dynamics in Ferromagnetic Nickel, *Phys. Rev. Lett.* **76**, 4250 (1996).
- [37] C. Berk, F. Ganß, M. Jaris, M. Albrecht, and H. Schmidt, All-optical measurement of interlayer exchange coupling in Fe/Pt/FePt thin films, *Appl. Phys. Lett.* **112**, 052401 (2018).
- [38] G. Wu, S. Chen, Y. Ren, Q. Jin, and Z. Zhang, Laser-Induced magnetization dynamics in interlayer-coupled [Ni/Co]₄/Ru/[Co/Ni]₃ perpendicular magnetic films for information storage, *ACS Appl. Nano Mater.* **2**, 5140 (2019).
- [39] M. Farle, T. Silva, and G. Woltersdorf, *Spin Dynamics in the Time and Frequency Domain*, (Magnetic Nanostructures: Spin Dynamics and Spin Transport Springer Berlin Heidelberg, Berlin, Heidelberg, 2013), p. 37.
- [40] A. Capua, S.-H. Yang, T. Phung, and S. S. P. Parkin, Determination of intrinsic damping of perpendicularly magnetized ultrathin films from time-resolved precessional magnetization measurements, *Phys. Rev. B* **92**, 224402 (2015).
- [41] M. Tang, W. Li, Y. Ren, Z. Zhang, S. Lou, and Q. Y. Jin, Magnetic damping and perpendicular magnetic anisotropy in Pd-buffered [Co/Ni]₅ and [Ni/Co]₅ multilayers, *RSC Adv.* **7**, 5315 (2017).
- [42] J. C. Rojas-Sánchez, N. Reyren, P. Laczkowski, W. Savero, J. P. Attane, C. Deranlot, M. Jamet, J. M. George, L. Vila, and H. Jaffres, Spin Pumping and Inverse Spin Hall Effect in Platinum: The Essential Role of Spin-Memory Loss at Metallic Interfaces, *Phys. Rev. Lett.* **112**, 106602 (2014).
- [43] B. L. Zink, M. Manno, L. O'Brien, J. Lotze, M. Weiler, D. Bassett, S. J. Mason, S. T. B. Goennenwein, M. Johnson, and C. Leighton, Efficient spin transport through native oxides of nickel and permalloy with platinum and gold overlayers, *Phys. Rev. B* **93**, 184401 (2016).
- [44] W. Zhang, W. Han, X. Jiang, S.-H. Yang, and S. S. P. Parkin, Role of transparency of platinum-ferromagnet interfaces in determining the intrinsic magnitude of the spin Hall effect, *Nat. Phys.* **11**, 496 (2015).

- [45] M. Battiato and K. Held, Ultrafast and Gigantic Spin Injection in Semiconductors, *Phys. Rev. Lett.* **116**, 196601 (2016).
- [46] H.-S. Song, K.-D. Lee, J.-W. Sohn, S.-H. Yang, S. S. P. Parkin, C.-Y. You, and S.-C. Shin, Observation of the intrinsic gilbert damping constant in Co/Ni multilayers independent of the stack number with perpendicular anisotropy, *Appl. Phys. Lett.* **102**, 102401 (2013).
- [47] L. Liu, T. Moriyama, D. C. Ralph, and R. A. Buhrman, Spin-torque Ferromagnetic Resonance Induced by the Spin Hall Effect, *Phys. Rev. Lett.* **106**, 036601 (2011).
- [48] L. Bai, P. Hyde, Y. S. Gui, C. M. Hu, V. Vlaminck, J. E. Pearson, S. D. Bader, and A. Hoffmann, Universal Method for Separating Spin Pumping From Spin Rectification Voltage of Ferromagnetic Resonance, *Phys. Rev. Lett.* **111**, 217602 (2013).
- [49] C.-F. Pai, Y. Ou, L. H. Vilela-Leão, D. C. Ralph, and R. A. Buhrman, Dependence of the efficiency of spin hall torque on the transparency of Pt/ferromagnetic layer interfaces, *Phys. Rev. B* **92**, 064426 (2015).
- [50] X. Tao, Q. Liu, B. Miao, R. Yu, Z. Feng, L. Sun, B. You, J. Du, K. Chen, S. Zhang, L. Zhang, Z. Yuan, D. Wu, and H. Ding, Self-consistent determination of spin hall angle and spin diffusion length in Pt and Pd: The role of the interface spin loss, *Sci. Adv.* **4**, eaat1670 (2018).